Investigation on Dynamical Mechanics of Rock-Backfill Composite Samples under SHPB Test

Haiyue Ma[1,2,3], Yunpeng Zhang[1,4,*] and Xiaodong Feng[2,3]

[1] College of Mining Engineering, North China University of Science and Technology, Tangshan, 063210, China

[2] College of Mechanical Engineering, Hebei University of Architecture, Zhangjiakou, 075000, China

[3] Hebei Technology Innovation Center for Intelligent Production Line of Prefabricated Building Components, Zhangjiakou, 075000, China

[4] Hebei Province Key Laboratory of Mining Development and Security Technology, Tangshan, 063210, China

INFORMATION

Keywords:
Split Hopkinson pressure bar (SHPB)
cemented tailings backfill (CTB)
dynamical characteristics
Numerical simulation

DOI: 10.23967/j.rimni.2025.10.71351

SCIPEDIA Revista Internacional de Métodos Numéricos para Cálculo y Diseño en Ingeniería

Revista Internacional Métodos numéricos para cálculo y diseño en ingeniería RIMNI in cooperation with CIMNE

Investigation on Dynamical Mechanics of Rock-Backfill Composite Samples under SHPB Test

Haiyue Ma[1,2,3], **Yunpeng Zhang**[1,4,*] **and Xiaodong Feng**[2,3]

[1]College of Mining Engineering, North China University of Science and Technology, Tangshan, 063210, China

[2]College of Mechanical Engineering, Hebei University of Architecture, Zhangjiakou, 075000, China

[3]Hebei Technology Innovation Center for Intelligent Production Line of Prefabricated Building Components, Zhangjiakou, 075000, China

[4]Hebei Province Key Laboratory of Mining Development and Security Technology, Tangshan, 063210, China

ABSTRACT

In blast-induced caving mining with backfilling, understanding the interaction mechanisms and deformation evolution between rock and cemented tailing backfill (CTB) under coupled conditions is essential for ensuring stability. This study conducted dynamic uniaxial impact tests using the Split Hopkinson Pressure Bar (SHPB) system on rock-CTB composite specimens to investigate their mechanical response at high strain rates. Stress–strain relationships were recorded across a range of strain rates, and corresponding failure mechanisms were analyzed. A coupled SHPB model was also developed using GDEM software to simulate internal stress wave propagation and crack evolution within the composite specimens. Experimental results revealed that the dynamic compressive strength initially increases, then decreases, and eventually stabilizes as the average strain rate (ASR) increases from 27.45 s^{-1} to 68.73 s^{-1}. At strain rates below 60 s^{-1}, the stress–strain curves exhibit a "stress drop" pattern, whereas above 60 s^{-1}, a "stress rebound" behavior is observed. Energy absorption increases with ASR up to 55 s^{-1}, then decreases, followed by a secondary increase. Numerical simulations validated the experimental findings, revealing the formation of both transverse and longitudinal cracks within the CTB. Greater deformation was observed near the transmission bar interface compared to the rock interface. These results offer valuable insights into the dynamic failure behavior of backfilled systems and inform improved backfill design in blast-induced mining operations.

OPEN ACCESS

Received: 05/08/2025

Accepted: 05/09/2025

Published: 03/02/2026

DOI
10.23967/j.rimni.2025.10.71351

Keywords:
Split Hopkinson pressure bar (SHPB)
cemented tailings backfill (CTB)
dynamical characteristics
Numerical simulation

1 Introduction

The practice of backfilling underground mining voids with leftover rock, crushed stone, tailings, and other materials is known as backfill mining. It is a crucial technique for extracting resources in an eco-friendly manner. In contrast to other mining techniques, backfill mining improves the stability

*Correspondence: Yunpeng Zhang (1309132@163.com).

of regions that have been dug out and stops major rock mass movement and surface subsidence brought on by mining operations. It gets rid of ecological harm, tailings, and waste rock occupancy that cause geological disasters and pollution to the environment [1–4]. It also drastically lowers dilution losses, limits tailings and waste rock outflow, and increases total resource recovery rates [5]. One of the main techniques used in underground mining operations is blasting. However, the unavoidable impact and vibration from blasting actions during backfill mining blasting operations negatively affect the stability of the backfill mass, altering its structural integrity. Using a uniaxial press, Li et al. [6] ascertained the mechanical characteristics of backfill materials with different cement-sand ratios. The ideal cement-sand ratio backfill was then entered into numerical models created by simulation software that mimicked real mine blasting and excavation. The study examined how various blasting sequences affected the bulk of the backfill and found that blasting simultaneously caused the least amount of backfill damage. Furthermore, one of the most important factors in improving blast resistance is the backfill material's ductility. Explosion seismic waves recorded at mining locations were used by Emad et al. [7] to calibrate FLAC3D simulation software models that simulate mining sequences. In addition, the models were updated to include real-world stress data from measurements. The analysis discovered that the top portions of the backfill in the mined-out area were experiencing wedge-shaped failures. In addition, the backfill mass's acceptable safe vibration levels were calculated.

With a strain rate ranging from 10 to 10^3 s^{-1}, the SHPB is utilized to study dynamic loads caused by explosions or impacts. This is used to model the impact loads that rocks encounter during real mine blasting operations, including situations where static loads are present first and dynamic loads are applied later [8–14]. Therefore, investigating the impact response of rocks and backfill using the Split Hopkinson Pressure Bar (SHPB) method is of great significance for understanding the propagation behavior of blasting waves and the stability of backfill. Previous studies have primarily focused on the effects of single materials or interfacial behavior on the impact response. Two cylindrical rock specimens were created by Li et al. [15], one of which had numerous grooves simulating rock joints on the contact side of the other specimen. The impact of contact area and spatial geometric shape on the propagation of explosive vibration waves was investigated using the SHPB experimental setup. On jointed rocks, it was found that the reflection coefficient is inversely related to the rock joint matching coefficient, while the wave propagation coefficient is directly proportional to the latter. However, such studies have mostly remained at the level of macroscopic experimental observations, lacking systematic comparison with wave impedance models, and have not yet been extended to complex CTB–rock composite systems. Tan et al. [16] used SHPB to perform impact studies on CTB at different ratios of sand to cement. Tensile failure and X-conjugate shear failure, akin to low-strength concrete, were found to be the failure mechanisms of the CTB at low-speed impact. There are four stages to the stress-strain curve of the CTB; some specimens show one or two lower stress peaks prior to fracture. The dynamic peak stress is directly proportional to the sand-to-cement ratio at the same impact velocity. Using scanning electron microscopy, Zheng et al. [17] studied the progression of cracks within the CTB during SHPB impact tests. It was discovered that as the ASR increases, the dynamic uniaxial compressive strength and energy absorption of the CTB first rise and subsequently fall. The side of the incident bar had substantially more cracks than the side of the transmission bar, according to micro-CT scans. Han and Li [18] used high-speed photography to capture the composite rock mortar specimens' SHPB impact test procedure. It was found that the layer of cement mortar acts as a cushion during deformation, and that tensile cracks spread in the direction of loading until the specimen's overall tensile failure. Xue et al. [19] used high-speed photography and SHPB to examine the dynamic properties of polypropylene fiber-containing CTB. The fiber-reinforced fill material's stress-strain curve showed a bimodal pattern, with the distance between the two stress peaks getting

smaller as the fiber content increased. In contrast to the instability failure brought on by stress in regular CTB, the fiber-reinforced fill showed edge spalling and core instability failure. These results suggest that dynamic fracture mechanics has potential explanatory power in describing the initiation and propagation of cracks in CTB; however, existing studies have not yet systematically incorporated it into the analytical framework.

During the two-step pillar mining process that employs the fill mining method, the impact load from the blasting process first affects the two-step pillar and then passes the energy and impact load to the CTB. Thus, it is equally important to understand the CTB and rock as a composite material. At the moment, several experimental investigations on coupled systems with CTB and rock have been carried out by academics. Selçuk and Aşma [20] performed point load, splitting tensile, and uniaxial compression tests on specimens of rock-concrete that had varying slopes. The tensile strength changed with the inclination angle under splitting tensile conditions, and there was a substantial link between the point load and interface inclination angle. Weilv et al. [21] produced samples of cemented paste back-fill-rock (CPB-rock) two interface angles and three distinct sand-to-cement ratios. After standard triaxial tests were carried out, it was discovered that the interface angle dominated the composite material's failure mode. The ratio of sand to cement directly correlated with the composite material's brittleness and variation in shear strength. A technique was put out to measure the effect on the composite material's stability of the interface be-tween CPB-rock. Yu et al. [22,23] conducted triaxial compression experiments to investigate specimens with CTB wrapping around rocks and rocks enveloping CTB. In comparison to rock specimens, both varieties of composite specimens demonstrated distinct post-peak stress platforms and greater residual strengths, which indicated strain softening proper-ties. The confining pressure and the volume percentage of the rock were directly correlated with the maximal strength of both composite specimens. The specimen with the boulders encasing the cement-filled tailings was more sensitive to the volume fraction at its maximal strength. The specimen with rocks encasing tailings-cemented fill had a lateral de-formation capacity that was significantly limited by the contact support between the rocks and fill, whereas the specimen with rocks encasing tailings-cemented fill only had a lateral deformation capacity that was related to the mechanical properties of the rocks. Using acoustic emission monitoring equipment, Wang et al. [24] kept an eye on specimens with rocks encasing CTB during uniaxial compression studies. It was discovered that fractures started out in the middle of the CTB and eventually spread to the surrounding rocks, failing as a whole. Based on the idea of energy conservation, a constitutive model of the composite material was created. The majority of these studies, meanwhile, only focus on static mechanical characteristics, and there is still more work to be done to fully characterize the mechanical characteristics of rock-CTB under the dynamic loading of blasting.

In summary, the current research exhibits two major limitations: (i) although previous studies have revealed certain behaviors of jointed rocks or CTB under dynamic loading, they have not sufficiently integrated wave impedance models and dynamic fracture mechanics to explain the mechanisms of wave propagation and failure in coupled systems; (ii) investigations on rock-CTB composites have largely been restricted to static loading, with a lack of systematic dynamic experimental data under varying strain rates. To address these gaps, this study focuses on rock-CTB composites and conducts SHPB dynamic uniaxial impact tests to obtain stress–strain characteristics at high strain rates. The failure process is further analyzed by integrating dynamic fracture mechanics and wave propagation theories, thereby providing both theoretical and experimental support for evaluating CTB stability under mining blasting conditions.

2 Materials and Methods

2.1 Sample Preparation

A strain rate that is less than or equal to 10^{-5} s^{-1} is referred to as "static". "Quasi-static" refers to strain rates that, in traditional static tests, typically range from 10^{-5} to 10^{-3} s^{-1} while concurrently ignoring the effects of strain rate. Under seismic stress circumstances, moderate strain rates are defined as those that fall between 10^{-3} and 10^{2} s^{-1}. High strain rates are defined as strain rates greater than 10^{2} s^{-1} [25].

This experiment primarily investigates the mechanical characteristics of rock-CTB specimens under high strain rates. Reflecting actual mining conditions, two types of CTB specimens were prepared with a cement-to tailings ratio (c/t) of 1:4 and a solid density (SD) 72%. One type consisted of standard Φ50 × 100 mm specimens, subjected to uniaxial compression tests. Another type was prepared with homemade molds into Φ50 × 25 mm backfill specimens [17] for SHPB dynamic compression strength testing. Rock specimens were obtained using a core drilling machine from a gold mine in Shandong, China, and were of granite type. Two types of rock specimens were prepared: standard Φ50 × 100 mm specimens for uniaxial compression tests and Φ50 × 25 mm specimens for SHPB dynamic compression strength testing. The wave velocities of both rock and backfill specimens were measured using a ultrasonic velocity gauge. This paper focuses on detailing the experimental procedures of the rock-filled coupling bodies under dynamic loading conditions. Table 1 presents the basic mechanical parameters of the backfill and rock.

Table 1: Mechanical parameters of backfill samples

	Height (mm)	Dimeter (mm)	Density (kg/m^3)	Uniaxial compressive strength (MPa)	Wave velocity (m/s)	Wave impedance ($kg/(m^2 \cdot s)$)
CTB	25 ± 0.3	50 ± 0.2	1880 ± 20	3.86	1950 ± 40	3.6 × 106
Rock	25 ± 0.3	50 ± 0.2	2838 ± 20	124.55	2860 ± 40	1.84 × 106

The aggregate used for CTB comes from the complete tailings of a gold mine in Shan-dong province, China, with a specific gravity of 2.85 g/cm^3. Analysis revealed a high SiO_2 content in the tailings, along with low amounts of CaO, MgO, S, P, and other components, as detailed in Table 2. Physicochemical analysis suggests that the tailings from this mine are a relatively inert backfill aggregate. The cementitious material selected is 32.5 Portland cement, and the mixing water is laboratory tap water.

Table 2: The chemical composition of full tailing

Chemical composition	TFe	SiO_2	Al_2O_3	CaO	MgO	S	P	Else
Content (wt.%)	5.43	72.17	6.38	4.71	4.02	0.196	0.16	6.974

The following instruments were employed in the experiment: electronic balance, basin, beaker, vernier caliper, cement mortar mixer, fully automatic standard constant temperature and humidity curing box, SHPB system, and others. A Φ50 × 25 mm acrylic cylindrical plastic tube mold was utilized, as illustrated in Fig. 1.

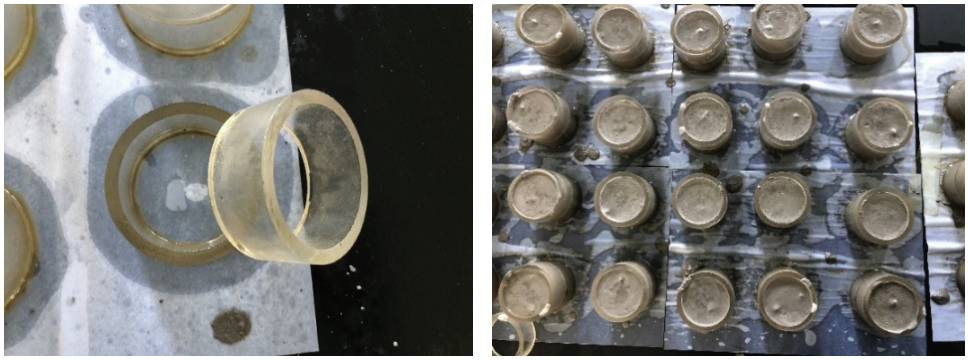

Figure 1: Mold and manufacture of CTB

This based on the concentration ratio set for the experiment, the required material quantities were calculated. The precise measurements of the raw materials were taken and placed into the mixer. After thorough mixing for at least 3 min [26], the mixture was poured into a basin. Before casting, a small amount of lubricating oil was applied to the interior of the mold using a brush to facilitate demolding of the backfill specimen. Simultaneously, a complementary mold was placed above the mold to ensure a successful single pouring. To prevent sedimentation of the slurry, it was stirred continuously during pouring, resulting in the cast backfill specimen as shown in Fig. 1. After 5 h, when the slurry began to set, the upper mold was removed, and the surface was smoothed. After 24 h, the backfill specimen was demolded and placed in a standard curing box for 28 days curing period at a temperature of 20°C and humidity greater than 90%. Upon completion of the curing period, as the SHPB experiment required the flatness of the specimen end faces to be less than 0.02 mm [27], a double-end grinding machine was used to grind both ends of the cured backfill specimen. Water was not added during the grinding process, as adding water could alter the mechanical parameters of the backfill specimen.

2.2 Experimental Devices

SHPB, originally designed by Hopkinson. B in the early 20th century, is a device used to test the dynamic performance of metal materials. It achieves different horizontal impact velocities by adjusting the impact air pressure. The Hopkinson experimental setup mainly consists of elastic waveguide bars, guide bar supports, base, stress wave generation device (nitrogen cylinder, bullet launch chamber, spindle-shaped bullet, pressure gauge), timer, ultra-dynamic strain gauge, oscilloscope, and computer. Fig. 2 below illustrates a schematic diagram of the Hopkinson experimental setup in the Dynamics Laboratory of North China University of Science and Technology. In the SHPB system, the material of the elastic waveguide bars is 40Cr alloy steel, with incident and transmitted bars having a length of 2000 mm and a diameter of 50 mm. The material density is 7800 kg/m^3, and the elastic modulus is 206 GPa, with a longitudinal wave velocity of 5198 m/s. Strain gauges of type BE120-2AA are selected and attached at positions equidistant from the specimen on the incident and transmitted bars to simultaneously measure the reflected and transmitted waves. The rock-CTB specimen is placed between the incident and transmitted bars, and the cylinder is set to generate impact air pressure. The measurement system automatically records the velocity of the bullet impacting the backfill material when fired. A high-precision dynamic testing analyzer collects and processes the shock wave data.

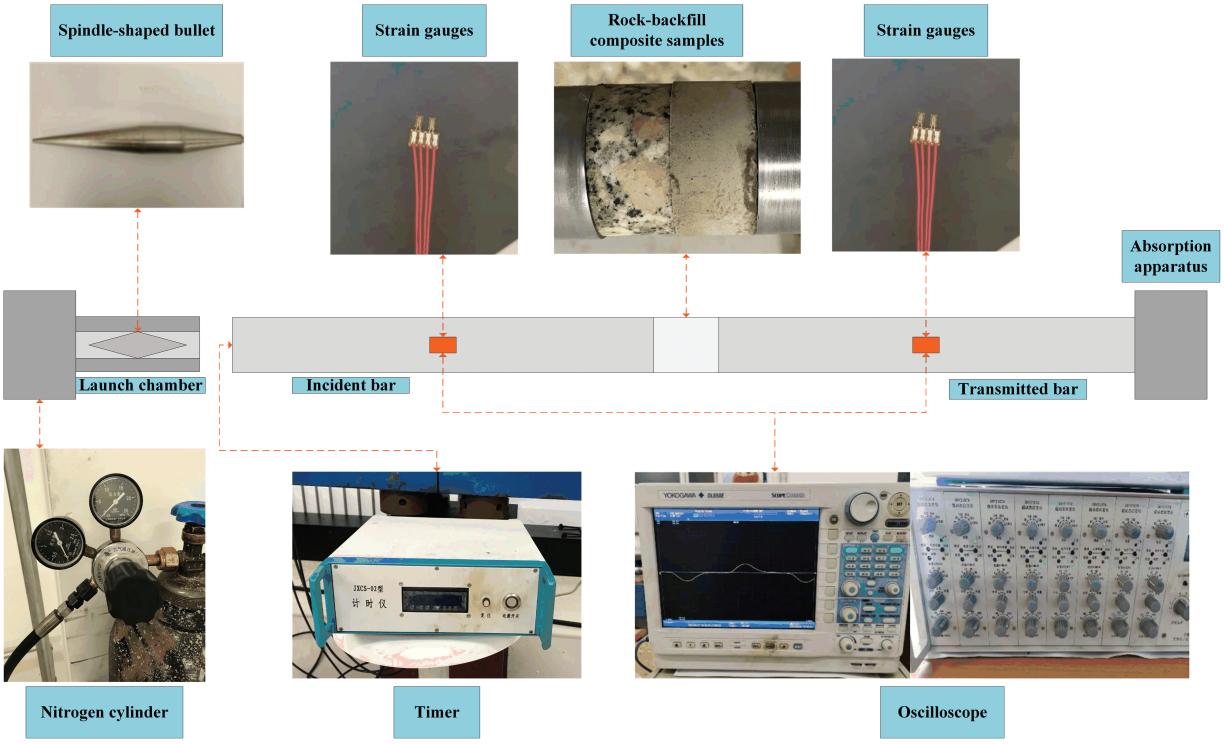

Figure 2: Schematic diagram of the SHPB device

2.3 Testing Program

In the process of impact, the rate at which the specimen undergoes overall deformation is referred to as the strain rate. In SHPB experiments, the average strain rate of the specimen is selected as the strain rate indicator. A method involving the adjustment of impact air pressure and the position of the projectile is employed to control the variation in impact velocity. Through preliminary experiments, the minimum velocity required for the projectile to exit is determined as the minimum value for uniaxial impact testing, while the maximum value is the impact velocity that leads to complete fragmentation of the specimen and loss of load-bearing capacity. For the current rock-CTB specimen, the range of impact velocities is set between 3 and 7 m/s.

A total of 35 rock-CTB specimens were fabricated and categorized into five groups for impact testing at projectile impact velocities of 3, 4, 5, 6, and 7 m/s. Each group consists of six rock-CTB specimens, and the remaining five sets of specimens are held as reserves to account for potential accidental damage during experiments. The specimen identification is structured as follows: impact velocity-specimen number.

The contact side of the incident bar and the transmitted bar with the specimen is coated with butter to reduce the influence of friction [27]. The rock and the CTB material are aligned at the center, tightly sandwiched between the incident and transmitted bars, ensuring a firm contact with the bars without sliding. In uniaxial impact loading of the coupled specimen, the incident bar is in contact with the rock side, and the transmitted bar is in contact with the filling material side. The collection box at the bottom of the specimen is cleaned and placed below the specimen. After placing the specimen, a transparent acrylic cover provided for the experiment is used to cover the specimen, preventing injury

from fragments generated during impact. When opening the valve, personnel should stay away from the SHPB experimental equipment to avoid accidental injury.

3 Results and Discussion

3.1 Dynamic Stress Equilibrium

Following the increase in incident velocity, the original waveform graphs of selected specimens (3-3, 4-6, 5-4, 6-4, 7-6) were obtained, as illustrated in Fig. 3a. It can be observed that the amplitude of the incident wave is roughly equal to that of the reflected wave, but they are in opposite directions, while the amplitude of the transmitted wave is relatively small. This indicates that only a small portion of the stress wave transmitted through the rock-CTB specimen is received by the transmitted bar, with the majority of energy being reflected, and only a small fraction of energy managing to pass through the specimen.

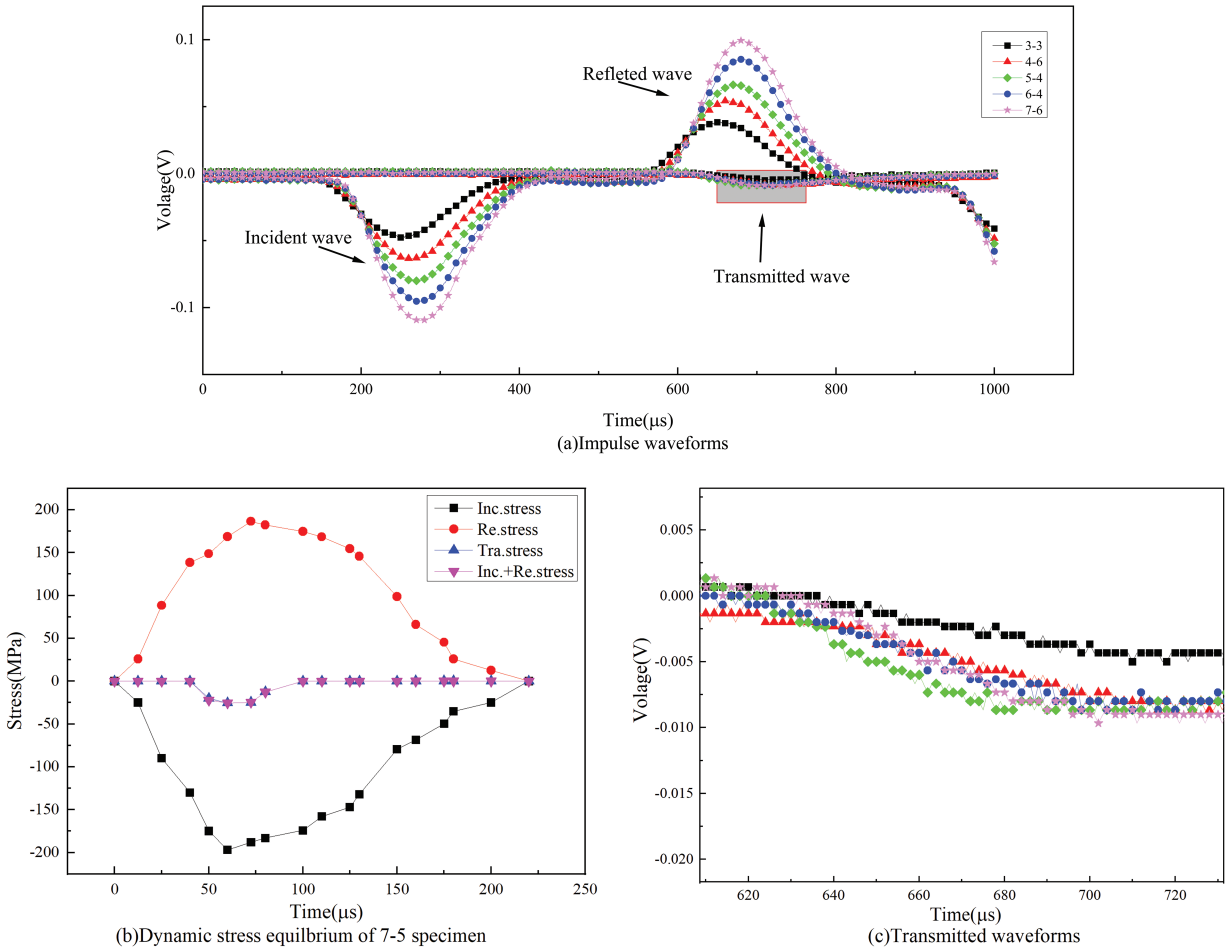

Figure 3: Partial sample original waveform

This is attributed to the significant differences in wave impedance among the rock, CTB, and the waveguide bars of the SHPB device. The filling material, composed of tailings, lime, and water, exhibits low density, numerous pores, and fine cracks, resulting in poor density and smaller wave velocity and impedance. Due to the substantial differences in wave impedance and elastic modulus between the

specimen and the pressure bars, regardless of whether the energy of the stress wave is increased or decreased, the incident wave cannot completely propagate through the interfaces on both sides due to the differing wave impedances. As the stress wave propagates through the rock-CTB specimens, it undergoes multiple changes in wave impedance, leading to a reduced energy of the transmitted wave.

The prerequisite for the SHPB experimental system is compliance with the one-dimensional stress wave propagation theory, and stress equilibrium at both ends of the specimen is a necessary condition. Therefore, it is essential to conduct a stress equilibrium test on the specimen. The stress waves from different parts of the waveform are shifted and superimposed. When the sum of the incident and reflected waves is approximately equal to the transmitted wave, it is considered that stress equilibrium is achieved at both ends of the specimen. As shown in Fig. 3b, the waveform graph of the 7-5 specimen is superimposed. The sum of the incident and reflected waves represents the stress at the incident end, and the transmitted wave represents the stress at the transmitting end. After shifting and superimposing, the relationship between stress and time at both ends of the pressure bars can be obtained. It can be observed that the superimposed wave and the transmitted wave overlap almost perfectly, with similar amplitudes, indicating that stress equilibrium has been achieved at both ends of the specimen.

3.2 Dynamic Compressive Strength Characteristics

The impact velocity of the spindle-shaped projectile can be calculated from the time collected by the timer. The incident stress amplitude can be obtained by multiplying the incident voltage amplitude by the conversion coefficient corresponding to the strain gauge model. After processing the raw data using the MySHPB software provided with the instrument, parameters such as the average strain rate and dynamic compressive strength of the coupled specimen can be determined. The SHPB experimental data for the rock-CTB specimen are presented in Table 3.

Table 3: Test results of mechanical properties of rock backfill under uniaxial impact

Specimen no.	Impact velocity (m/s)	ASR (s^{-1})	Incident stress (MPa)	Dynamic compressive strength (MPa)
3-3	3.12	27.45	48.16	1284.70
3-5	3.51	29.46	55.53	1407.00
4-6	4.00	37.75	64.62	2383.30
5-4	5.08	46.80	80.77	589.26
6-2	5.73	54.81	92.88	635.67
6-5	5.88	56.39	92.88	431.44
6-3	5.91	57.44	92.88	662.62
6-4	6.03	59.53	96.22	630.56
7-2	6.53	63.38	106.01	491.37
7-6	7.08	68.73	111.06	588.77

The impact velocity of the spindle-shaped projectile can be calculated from the time collected by the timer. The incident stress amplitude can be obtained by multiplying the incident voltage amplitude by the conversion coefficient corresponding to the strain gauge model. After processing the raw data using the MySHPB software provided with the instrument, parameters such as the average

strain rate and dynamic compressive strength of the coupled specimen can be determined. The SHPB experimental data for the rock-CTB specimen are presented in Table 3.

Fig. 4 depicts the relationship between the average strain rate of rock-CTB specimens and impact velocity. As observed from the graph, with the increase in impact velocity, the average strain rate of rock-CTB specimens also increases, reaching a maximum of 68.73 s^{-1}. This trend exhibits a linear positive correlation, and Eq. (1) represents the fitted relationship, with a coefficient of determination $R^2 = 0.994$.

$$\dot{\varepsilon} = 10.74v - 6.59 \tag{1}$$

The dynamic compressive strength of rock-CTB specimens exhibits a trend of initially increasing, then decreasing, and eventually stabilizing with the rise in average strain rate. When the average strain rate is less than 45 s^{-1}, a significant strain rate effect is evident in rock-CTB specimens, characterized by a rapid variation in strain rate. In this regime, the dynamic compressive strength rapidly increases with the augmentation of the average strain rate. For instance, within the range of 27 to 38 s^{-1}, there is a 41% increase in strain rate, resulting in a surge of dynamic compressive strength from 1284.7 to 2383.3 MPa, marking an 86% increment. Beyond an average strain rate of 45 s^{-1}, the rock-CTB specimens approach the ultimate carrying limit of the impact load, and the dynamic strength tends to stabilize. Within the range of 49 to 69 s^{-1}, a 41% increase in strain rate is observed. However, the dynamic compressive strength experiences a marginal decrease from 406.43 to 405.01 MPa, reflecting a minimal reduction of 0.03%. The strain rate effect diminishes as the average strain rate exceeds 45 s^{-1}. Utilizing Gaussian fitting provides a satisfactory expression for the relationship between dynamic compressive strength and average strain rate. The fitted curve aligns well with the data, as represented by Eq. (2), with a coefficient of determination $R^2 = 0.9545$.

$$y = 567.56 + \frac{24630.1e^{-2\left(\frac{x-35.33}{9.7}\right)^2}}{9.7\sqrt{\frac{\pi}{2}}} \tag{2}$$

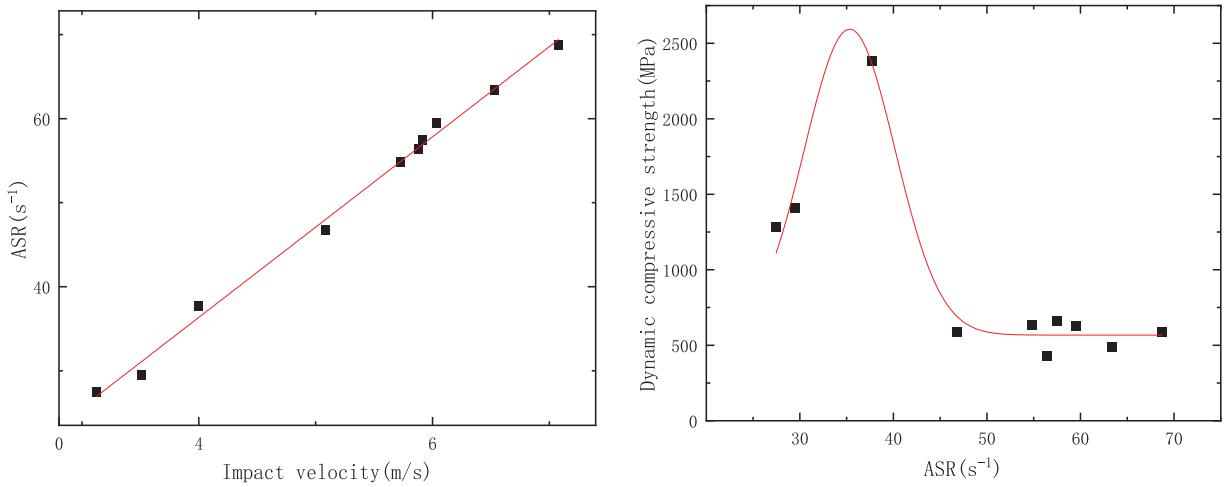

Figure 4: The relationship between average strain rate and impact velocity and dynamic compressive strength

3.3 Deformation Characteristics Analysis

The stress-strain curve can reflect the deformation characteristics of the specimen during impact loading. As shown in Fig. 5, the stress-strain curve of the rock-CTB specimen at a strain rate of 46.80 s^{-1} can be roughly divided into three stages: linear elastic stage (OA), nonlinear yielding stage (AB), and failure stage (BC).

In the OA stage, the loading rate of the impact is extremely high, and most of the energy absorbed by the specimen is converted into internal elastic strain energy, with the specimen exhibiting linear elastic deformation as a whole. Stress concentrations occur near the initial microcracks, while a small portion of the energy is dissipated to drive microcrack nucleation and development. This process can be interpreted by linear elastic fracture mechanics (LEFM), where microcracks accumulate damage under stress concentration without propagating into unstable cracks. During the AB stage, the specimen enters the nonlinear yielding region. The accumulated strain energy is gradually released and transformed into the dissipated energy required for crack propagation. Initial microcracks continue to extend, and new cracks are generated, leading to progressive material damage until the peak strength is reached at point B. This process is consistent with the "critical strain energy release rate" theory in dynamic fracture mechanics, indicating that crack propagation under high strain rates depends not only on the applied stress but also on the rate of energy release. In the BC stage, cracks further propagate and coalesce, eventually forming macroscopic cracks parallel to the loading direction, resulting in tensile splitting failure. This behavior is consistent with the interface weakening mechanism in composite materials: due to the mechanical property differences between rock and the CTB material, stress concentrations readily induce failure at the rock-CTB interface and within the filling material.

The stress-strain curves of rock-CTB specimens under different strain rates, as illustrated in Fig. 5, reveal slight variations in deformation characteristics before the dynamic peak strength and present two distinct types after the dynamic peak: "stress drop" and "stress rebound." For strain rates below 50 s^{-1}, the "stress drop" type curve is observed, where the specimen strain remains relatively constant, and stress rapidly decreases after reaching the peak. Combining this observation with the information in Table 4, it is inferred that no catastrophic failure occurred during loading, and the specimen retains partial load-bearing capacity. After reaching the peak strength, internal microcracks develop, surface cracking occurs, and irreversible deformation ensues. Consequently, stress rapidly declines to residual strength, while strain remains relatively constant. This phenomenon can be explained by stress wave transmission and attenuation theory. At relatively low strain rates, the energy exchange between reflected and transmitted waves is limited, and the crack propagation rate is insufficient to trigger a recovery of secondary load-bearing capacity. When the strain rate reaches approximately 60 s^{-1}, a "stress rebound" type curve appears, characterized by a stress drop after the peak followed by a secondary rise. This behavior arises because the wave impedances of the rock and the CTB material differ by an order of magnitude, causing strong reflection of the incident wave at the interface between the two media. Part of the stress wave is reflected back onto the specimen, resulting in localized stress re-concentration. The CTB material, having a lower strength than the rock, fails preferentially and exhibits a conical failure pattern, with the residual area on the side contacting the rock larger than that on the side in contact with the transmission bar. This phenomenon can be attributed to the multiple reflection–superposition effect of stress waves in composite materials. The impedance mismatch at the interface causes local energy re-accumulation, producing a "secondary loading" effect, which manifests as stress rebound on the stress–strain curve. When the strain rate exceeds 60 s^{-1}, the stress rebound becomes more pronounced, as most of the elastic energy absorbed by the rock is transferred to the CTB material. Due to the lower compressive strength of the CTB material compared to the rock, it undergoes comminution failure and loses load-bearing capacity. This observation indicates that under

high strain rate conditions, the failure mechanism of the composite system shifts to a brittle mode induced by energy concentration.

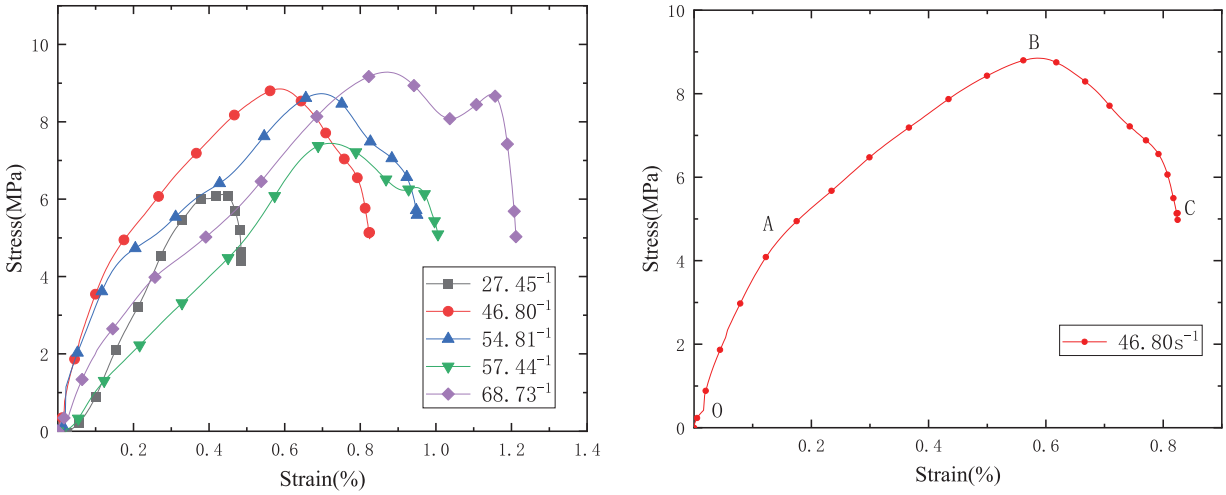

Figure 5: Stress-strain curves of coupled body at different strain rates

Table 4: Failure form and evaluation table of some rock backfill coupled body

Group number	ASR (s^{-1})	Form	Evaluation
3-3	27.45	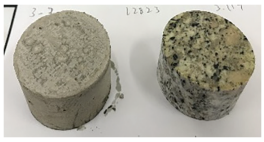	The rock specimens and filling material specimens remain intact.
4-5	41.77	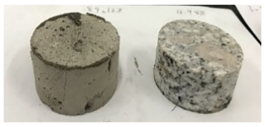	The rock specimens are intact, while radial and axial cracks appear in the filling material specimens. Macroscopically, the specimens remain stable.
5-4	46.80		The rock specimens remain intact, while the filling material specimens exhibit an increased number of radial and axial cracks. Spalling occurs on the side in contact with the transmission rod, but macroscopically, the specimens remain stable.

(Continued)

Table 4 (continued)

Group number	ASR (s^{-1})	Form	Evaluation
6-3	57.44	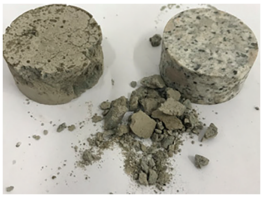	The rock specimens remain intact, while the filling material undergoes fragmentation. There is an increased occurrence of spalling on the side in contact with the transmission rod. However, some load-bearing capacity is still retained.
7-1	60.73		The rock specimens remain intact, while the filling material undergoes extensive fragmentation, exhibiting a conical shape. The remaining area on the side in contact with the transmission rod is smaller than on the side in contact with the rock. However, some residual strength is retained.
7-6	68.73		The rock specimens exhibit minor axial cracks, while the filling material undergoes fragmentation, experiencing complete instability.

3.4 Failure Form Analysis

The failure modes of rock-CTB specimens under single impacts at different strain rates in the SHPB apparatus vary, as indicated in Table 4.

At an average strain rate of 27.45 s^{-1}, both the rock and filling material specimens remain intact. As the average strain rate increases to 41.77 s^{-1}, cracks begin to appear in the filling material specimens, yet a significant portion of strength is retained, while the rock specimens remain intact. Further, at an average strain rate of 46.80 s^{-1}, the degree of cracking and damage in the filling material increases, with some spalling occurring on the side in contact with the transmission rod. However, the rock specimens remain intact. As the average strain rate further rises to 57.44 s^{-1}, the extent of cracking and damage in the filling material significantly increases, accompanied by an increased level of spalling, yet some load-bearing capacity is retained. The rock specimens remain intact. Upon reaching an average strain

rate of 60.73 s^{-1}, the filling material experiences fragmentation and instability, presenting a conical shape. The area in contact with the transmission rod is smaller than the area in contact with the rock. However, the rock specimens remain intact. At an average strain rate of 68.73 s^{-1}, the filling material undergoes complete fragmentation and instability, losing its load-bearing capacity, while the rock specimens exhibit minor cracking. In summary, the critical strain rate for the filling material to undergo fragmentation and instability is in the range of 50 to 60 s^{-1}. Analyzing the stress-strain curves within the experimental parameter range, it can be concluded that the critical strain rate for filling material fragmentation and instability in rock-CTB specimens is around 55 s^{-1}.

The transition from the 'stable crack growth stage' to the 'unstable fragmentation stage' reveals the emergent characteristics of the composite system: once the micro-damage evolution in the CTB reaches a critical threshold, it triggers a nonlinear mutation in the macroscopic mechanical response. Such phenomena not only reflect the redistribution of energy between the rock and the CTB, but also indicate that, at higher strain rates, the rock component gradually assumes the role of energy absorption, with the dominant energy-dissipating unit shifting from the CTB to the surrounding rock. This dynamic coupling mechanism provides experimental evidence for understanding the layered damage patterns and multi-scale energy dissipation behavior of composites under impact loading.

3.5 Energy Dissipation Analysis

In accordance with the law of conservation of energy, it is imperative to recognize that the deformation and failure process of rock-CTB specimens inherently involves changes in energy. In the field of dynamics, the assessment of energy variation in impact experiments for rock-CTB specimens is commonly expressed in terms of absorbed energy. The relationship among incident energy (W_1), reflected energy (W_R), transmitted energy (W_T, and absorbed energy (W_S) can be articulated as follows [12]:

$$W_1 = ACE \int_0^t \varepsilon_i^2(t)dt \tag{3}$$

$$W_R = ACE \int_0^t \varepsilon_r^2(t)dt \tag{4}$$

$$W_T = ACE \int_0^t \varepsilon_t^2(t)dt \tag{5}$$

$$W_S = W_1 - W_R - W_T \tag{6}$$

Here, A represents the cross-sectional area of the incident rod, C is the elastic stress wave velocity, E is the elastic modulus of the waveguide rod, ε_i is the incident strain, ε_r is the reflected strain, and ε_t is the transmitted strain. In accordance with the experimental findings, the energy characteristics of the rock-CTB coupled specimens are presented in Table 5.

Table 5: Energy calculation results of rock-CTB specimen SHPB experiment

Specimen identification	ASR (s^{-1})	Incident energy (J)	Reflected energy (J)	Transmitted energy (J)	Absorbed energy (J)
3-3	27.45	9.19	7.58	0.19	1.41
3-5	29.46	12.04	8.76	0.54	2.74
4-6	37.75	22.09	18.04	0.7	3.35

(Continued)

Table 5 (continued)

Specimen identification	ASR (s^{-1})	Incident energy (J)	Reflected energy (J)	Transmitted energy (J)	Absorbed energy (J)
5-4	46.80	26.45	22.11	0.59	3.75
6-2	54.81	34.38	29.91	0.52	3.95
6-5	56.39	37.11	33.3	0.31	3.5
6-3	57.44	35.95	33.14	0.35	2.41
6-4	59.53	38.1	34.91	0.37	2.82
7-2	63.38	46.62	42.57	0.43	3.62
7-6	68.73	52.53	46.33	0.57	5.63

As depicted in Fig. 6, a relationship chart between average strain rate and absorbed energy, incident energy, reflected energy, and transmitted energy was constructed based on the data presented in Table 5. It can be observed that incident energy and reflected energy exhibit a proportional relationship with the average strain rate of the rock-CTB specimen. When the average strain rate is below 54.81 s^{-1}, absorbed energy increases with the rise in average strain rate. In the range of average strain rates from 54.81 to 68.73 s^{-1}, absorbed energy first decreases and then increases. Absorbed energy reaches a minimum at an average strain rate of 57.44 s^{-1}, coinciding with the experimental observation that the filling material specimen has experienced spalling, losing its load-bearing capacity. At this point, the absorbed energy has reached its limit, indicating an inability to absorb more energy. As the average strain rate continues to increase, the filling material specimen absorbs a certain amount of energy before failure. During this phase, only the rock specimen absorbs energy, illustrating the process of increased energy absorption with the rise in average strain rate. It is noteworthy that the transmitted energy is consistently less than 1 J. This is attributed to the significant impedance mismatch between the rock, filling material, and the incident rod [17], resulting in minimal stress wave reception by the transmitted rod. As a consequence, the transmitted energy is negligible.

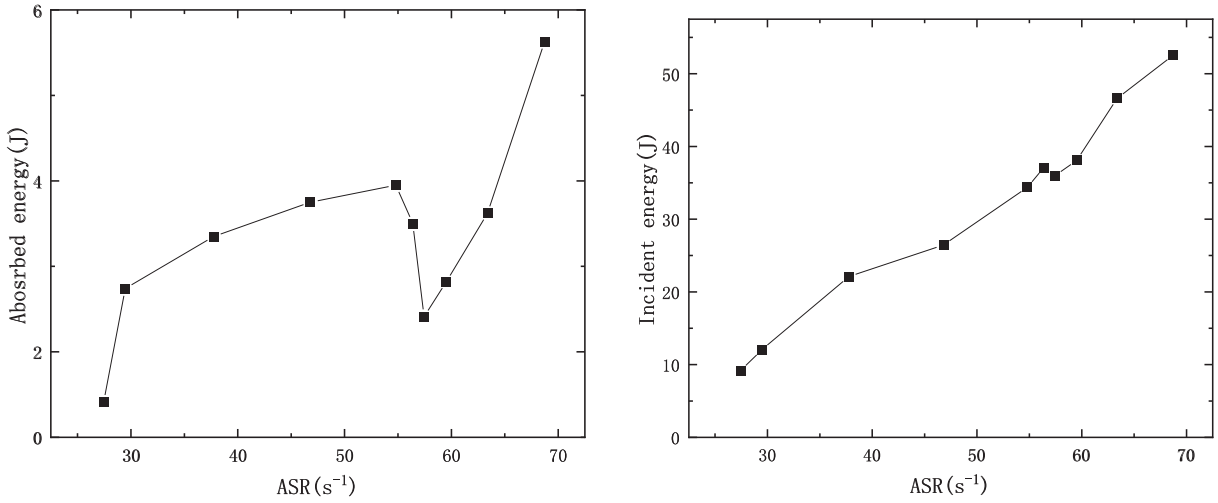

Figure 6: (Continued)

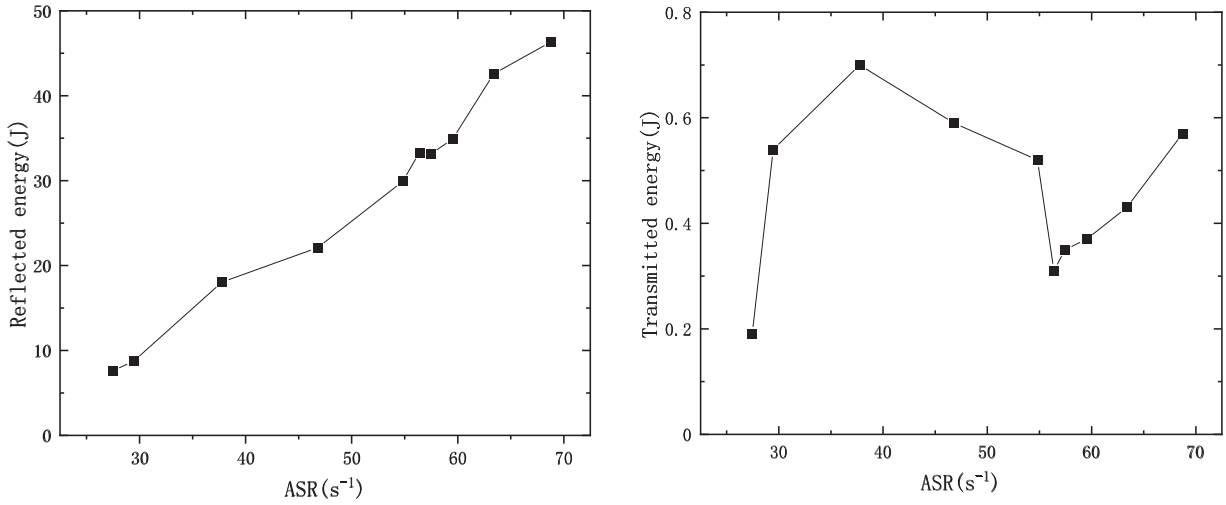

Figure 6: Diagram of energy change of rock-CTB specimen at different strain rates

4 Numerical Simulation of the Mechanical Properties of Rock-CTB Specimens

4.1 Simulation Methods and Parameters

As shown in Fig. 7, a numerical model of the filling material specimen with a diameter of 50 mm and thickness of 50 mm was established. Simultaneously, numerical models of incident and transmitted rods, both with a diameter of 50 mm and length of 2 m, were created. A spindle-shaped projectile was employed to impact the incident rod, generating stress waves to achieve constant strain rate loading. The simulation initiated by applying an initial velocity on the left side of the striker. After a certain duration, the striker collided head-on with the end of the incident rod at a set velocity, generating a sinusoidal wave similar to the SHPB experimental setup. Different impact velocities were utilized to achieve various strain rates. The model was discretized with 397,688 tetrahedral elements. The simulation duration for each case was 1.2 ms, and the end of the transmitted rod was set as a transparent boundary to replicate the effects of the absorptive rod and cushioning device in the experiment.

Figure 7: Diagram of energy change of rock-CTB specimen at different strain rates

During the numerical model simulations, the parameters for the filling material and rock were determined based on measurements from the experiments.

The CTB has a density of 2000 kg/m^3, an elastic modulus of 2.84 GPa, a Poisson's ratio of 0.3, normal and tangential stiffness of 1×10^8 MPa/m each, cohesive strength of 2.02 MPa, an internal friction angle of 35°, and tensile strength of 0.84 MPa.

The rock has a density of 3300 kg/m^3, an elastic modulus of 27 GPa, a Poisson's ratio of 0.2, cohesive strength of 11 MPa, an internal friction angle of 65°, and tensile strength of 10 MPa. These experimentally measured parameters were employed in the numerical calculations.

4.2 Model Establishment

The rock-CTB specimen was established in GDEM as illustrated in Fig. 8. Both the filling material and the rock have a length of 25 mm and a diameter of 50 mm. One end of the rock is in contact with the incident rod, while one end of the filling material is in contact with the transmitted rod, faithfully replicating the impact experiment described in Section 3. On the upper surface, fiv e monitoring points (designated as points 1 to 5) were set at 1 cm intervals along the axial direction from the center. The projectile's impact velocity was set at 3 m/s.

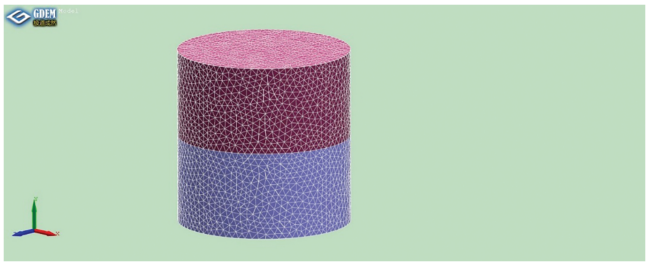

Figure 8: The backfill rock coupling model with direct contact between backfill and rock

4.3 Simulation Methods and Parameters

The axial velocity time history curves for monitoring points 1 to 5 are depicted in Fig. 9.

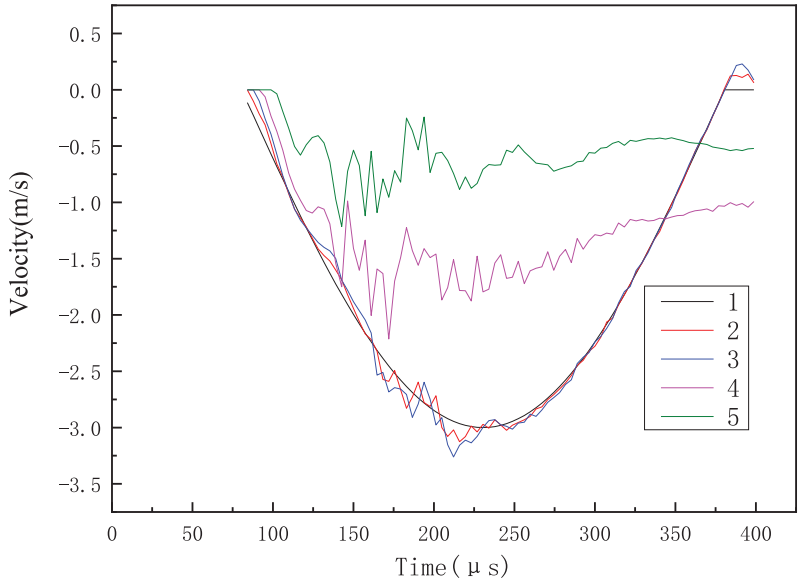

Figure 9: Time history curve of vibration velocity in vertical direction

From Fig. 9, it can be observed that the waveforms of the three monitoring points located on the rock are essentially consistent. Points 2 and 3 exhibit larger fluctuations, indicating that the rock

experiences axial velocity fluctuations due to the reflective effect from the CTB. Monitoring point 3 on the rock has a relatively large axial velocity, measuring 3.26 m/s. In the CTB, the axial velocity is greater on one side facing the rock, and the fluctuation pattern is more consistent. The peak axial velocity in the axial direction is 2.12 m/s.

From Fig. 10, it is evident that at 109.77 μs, the incident wave has propagated from the rock to the CTB. Micro-cracks start to form on the side of the CTB in contact with the rock. As time progresses, these cracks gradually develop. By 400 μs, both lateral and longitudinal cracks appear on the surface of the CTB, resulting in slight deformation. The surface area on the side in contact with the transmitted rod is greater than that on the side in contact with the rock. The maximum displacement of the rock is 0.55 mm, while the maximum displacement of the CTB occurs on the side in contact with the transmitted rod, measuring 0.14 mm.

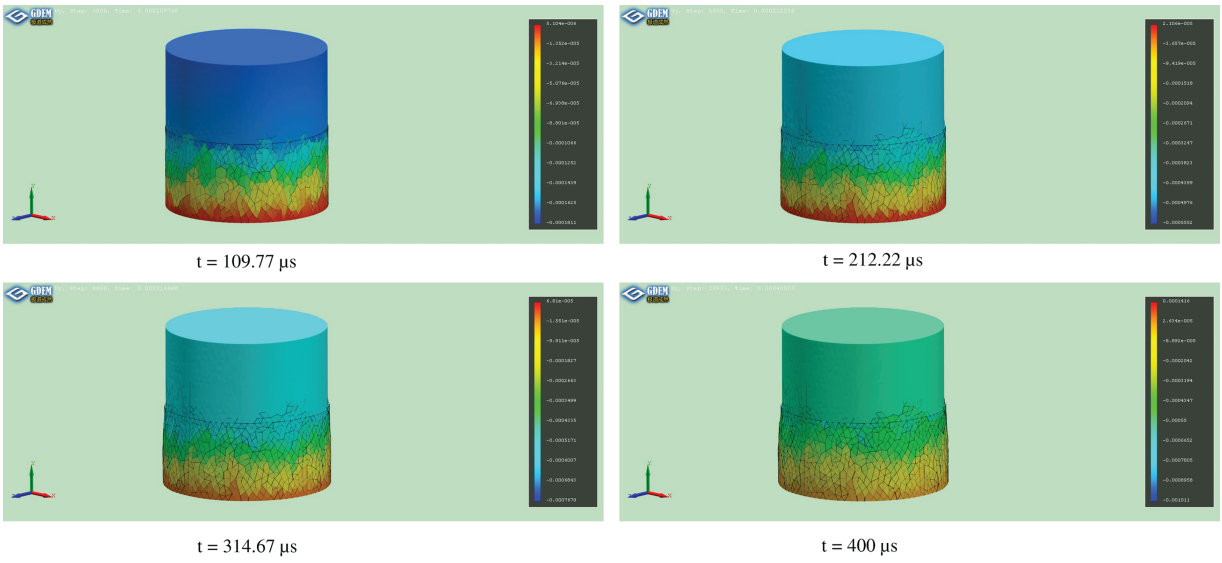

Figure 10: Vertical displacement diagram

Combining the data from Figs. 11 and 12, the analysis reveals that the axial stress variation trends for the rock and CTB are essentially consistent before 300 μs. However, after 300 μs, the axial stress of the rock exhibits directional fluctuations, possibly due to the reflective effect of the CTB. The magnitude of axial stress fluctuations in the CTB is smaller compared to that in the rock, and the stress reduction occurs earlier in the CTB, possibly due to its lower density and its capacity to absorb energy. The peak axial stress for the rock occurs at point 1, measuring 8.92 MPa, while for the CTB, it appears at point 4, measuring 2.82 MPa. Before 100 μs, the radial stress in the CTB is opposite in direction to that in the rock, and the radial stress in the CTB is larger than that in the rock. From 100 to 300 μs, the maximum radial stress is observed at monitoring point 3, possibly due to the frictional force between the rock and the CTB. After 300 μs, the trends in stress variation among the five monitoring points become consistent. The peak axial stress for the rock is located at point 1, measuring 9.69 MPa, while for the CTB, it is at point 5, measuring 7.84 MPa. The peak radial stress for the rock occurs at point 2, measuring 1.41 MPa, whereas for the CTB, it is at point 4, measuring 2.82 MPa.

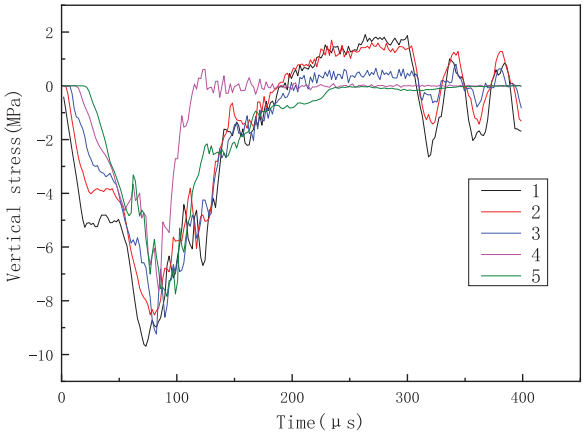

Figure 11: Stress time history curve in the vertical direction

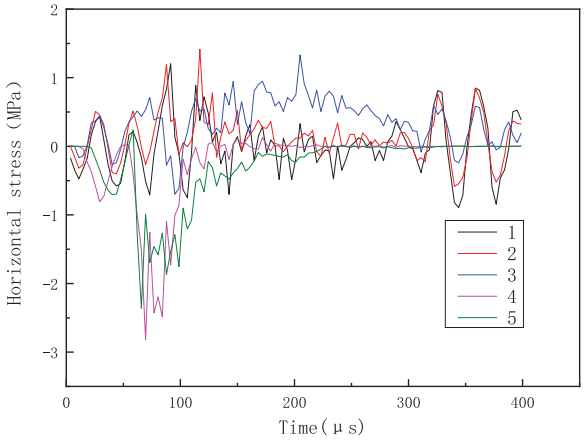

Figure 12: Horizontal stress time history curve

The numerical simulations not only agree with the experimental results in terms of the stress–strain evolution trends, but also reveal the meso-scale failure mechanisms within the composite system. The simulations indicate that crack initiation and propagation at the rock-CTB interface play a dominant role during stress wave transmission, which is closely related to the advantages of the discrete element method (DEM) in capturing crack evolution and energy dissipation characteristics. Nevertheless, the present modeling still has certain limitations: (i) the interface conditions between rock and CTB were simplified, without fully accounting for actual roughness and bonding heterogeneity; (ii) the material parameters were primarily determined from macroscopic mechanical tests, while sensitivity analyses of meso-scale parameters remain insufficient; and (iii) although GDEM can effectively describe crack evolution, it inevitably idealizes the propagation of stress waves in continuous media.

From a theoretical perspective, the numerical results highlight a ‘threshold effect’: when stress fluctuations in the CTB exceed a certain level, the associated energy absorption and crack evolution induce nonlinear mutations in the macroscopic stress–strain response. This phenomenon is consistent with continuum mechanics principles of stress wave scattering, interfacial friction, and energy redistribution in composite media. Therefore, the integration of experimental and numerical approaches not

only validates the energy absorption and dissipation functions of the CTB, but also provides important insights into the mechanisms of stress wave propagation and fracture evolution in rock-CTB systems.

5 Conclusion

In this study, a series of experiments were conducted on rock-CTB specimens, including SHPB uniaxial impact tests, energy dissipation tests, and computer numerical simulation experiments, to explore their dynamic mechanisms and deformation evolution characteristics. The conclusions drawn are as follows:

(1) In the SHPB experiments, the amplitude of the transmitted wave is nearly equal to the superimposed wave of the incident and reflected waves, with their waveforms overlapping. Stress equilibrium is achieved at both ends of the rock-filled specimens.

(2) When the average strain rate of the rock-CTB specimen ranges from 27.45 to 68.73 s^{-1}, the impact velocity increases with the increase in average strain rate, while the dynamic compressive strength shows an initial increase followed by a decrease before stabilizing as the average strain rate rises.

(3) The stress-strain curve of the rock-CTB specimen exhibits a "stress drop" type below an average strain rate of 60 s^{-1}, while it demonstrates a "stress rebound" type above 60 s^{-1}.

(4) The incident energy and reflected energy of the rock-CTB specimen increase with the increase in average strain rate, while the absorption energy shows an initial increase, followed by a decrease before increasing again. Transmitted energy can be neglected.

(5) Utilizing GDEM software, the SHPB uniaxial impact process of the rock-CTB specimen was simulated. The simulation results revealed the occurrence of both lateral and longitudinal cracks on the surface of the filling material. Deformation on the side of the filling material in contact with the transmitted rod was greater than that on the side in contact with the rock, thus validating the correctness of the experimental conclusions.

This study provides important guidance for optimizing the blasting-induced ore caving process in CTB mining. By clarifying the dynamic characteristics of the rock-CTB system, it offers a theoretical basis for the rational design of CTB strength and mix proportions, the control of blasting energy input, and the reduction of surrounding rock damage. Moreover, the results supply experimental support for establishing constitutive models and numerical simulations under complex coupling conditions. In the future, the proposed methods and findings may be extended to other engineering fields, such as tunnel excavation, underground energy storage, and seismic dynamic response, thereby offering new approaches for evaluating the stability and engineering applications of rock-CTB systems under dynamic loading.

Despite these advances in revealing the dynamic behavior and failure mechanisms of rock-CTB composites at high strain rates, several issues remain to be addressed. First, this study focused on a single mix proportion of the CTB; future work should consider the effects of different cementing agents, mix ratios, and curing ages on the dynamic performance of the composites to build a more comprehensive mechanical property database. Second, the present experiments were limited to uniaxial impact loading, whereas actual mining conditions are more complex. Future investigations should incorporate triaxial loading, cyclic impacts, and multi-field coupling to better approximate *in-situ* conditions. Finally, integrating laboratory results with field monitoring and industrial-scale tests will be essential to bridge the gap between experiments and practice, thereby supporting the safe and efficient application of CTB mining in complex underground environments.

Acknowledgement: Not applicable.

Funding Statement: This study was funded by the Hebei Province Nature Foundation Project (No. E2016209388).

Author Contributions: The authors confirm contribution to the paper as follows: Conceptualization, Yunpeng Zhang; methodology, Haiyue Ma; writing—original draft preparation, Haiyue Ma; writing—review and editing and supervision, Yunpeng Zhang, Haiyue Ma and Xiaodong Feng; funding acquisition, Yunpeng Zhang. All authors reviewed the results and approved the final version of the manuscript.

Availability of Data and Materials: Not applicable.

Ethics Approval: Not applicable.

Conflicts of Interest: The authors declare no conflicts of interest to report regarding the present study.

References

1. Li M, Peng Y, Ding L, Zhang J, Ma D, Huang P. Analysis of surface deformation induced by backfill mining considering the compression behavior of gangue backfill materials. Appl Sci. 2023;13(1):160. doi:10.3390/app13010160.
2. Gao R, Wang W, Xiong X, Li J, Xu C. Effect of curing temperature on the mechanical properties and pore structure of cemented backfill materials with waste rock-tailings. Constr Build Mater. 2023;409(96):133850. doi:10.1016/j.conbuildmat.2023.133850.
3. Du X, Feng G, Qi T, Guo Y, Zhang Y, Wang Z. Failure characteristics of large unconfined cemented gangue backfill structure in partial backfill mining. Constr Build Mater. 2019;194(11):257–65. doi:10.1016/j.conbuildmat.2018.11.038.
4. Zhao L. Numerical investigation on the mechanical behaviour of combined backfill-rock structure with KCC model. Constr Build Mater. 2021;283(2):122782. doi:10.1016/j.conbuildmat.2021.122782.
5. Huang Z, Cao S, Yilmaz E. Microstructure and mechanical behavior of cemented gold/tungsten mine tailings-crushed rock backfill: effects of rock gradation and content. J Environ Manag. 2023;339(2):117897. doi:10.1016/j.jenvman.2023.117897.
6. Li G, Deng G-Z, Ma J. Numerical modelling of the response of cemented paste backfill under the blasting of an adjacent ore stope. Constr Build Mater. 2022;343(4):128051. doi:10.1016/j.conbuildmat.2022.128051.
7. Emad MZ, Mitri H, Kelly C. Dynamic model validation using blast vibration monitoring in mine backfill. Int J Rock Mech Min Sci. 2018;107(4):48–54. doi:10.1016/j.ijrmms.2018.04.047.
8. Jang TJ, Yoon JW, Kim JB. Determination of Johnson-Cook constitutive model coefficients considering initial gap between contact faces in SHPB test. J Mater Res Technol. 2023;24:7242–57. doi:10.1016/j.jmrt.2023.05.001.
9. Wang J, Ma L, Zhao F, Lv B, Gong W, He M, et al. Dynamic strain field for granite specimen under SHPB impact tests based on stress wave propagation. Undergr Space. 2022;7(5):767–85. doi:10.1016/j.undsp.2021.11.010.
10. Zhou X, Xie Y, Long G, Zeng X, Li N, Ma G, et al. Multi-scale modeling of the concrete SHPB test based on DEM-FDM coupling method. Constr Build Mater. 2022;356(11):129157. doi:10.1016/j.conbuildmat.2022.129157.

11. Ren L, Yu X, Guo Z, Xiao L. Numerical investigation of the dynamic increase factor of ultra-high performance concrete based on SHPB technology. Constr Build Mater. 2022;325(1):126756. doi:10.1016/j.conbuildmat.2022.126756.
12. Li J, Yang L, Xie H, Wei P, Li D, Xu Y, et al. Research on impact toughness and crack propagation of basalt fiber reinforced concrete under SHPB splitting test. J Build Eng. 2023;77(1):107445. doi:10.1016/j.jobe.2023.107445.
13. Lv Y, Wu L, Su Y. SHPB experiments and FDM-DEM coupled simulations on calcareous sand under uniaxial to triaxial deformation. Int J Impact Eng. 2023;181(4):104751. doi:10.1016/j.ijimpeng.2023.104751.
14. Liu F, Li QM. Strain-rate effect of polymers and correction methodology in a SHPB test. Int J Impact Eng. 2022;161:104109. doi:10.1016/j.ijimpeng.2021.104109.
15. Li JC, Li NN, Li HB, Zhao J. An SHPB test study on wave propagation across rock masses with different contact area ratios of joint. Int J Impact Eng. 2017;105(6):109–16. doi:10.1016/j.ijimpeng.2016.12.011.
16. Tan Y-Y, Yu X, Elmo D, Xu L-H, Song W-D. Experimental study on dynamic mechanical property of cemented tailings backfill under SHPB impact loading. Int J Miner Metall Mater. 2019;26(4):404–16. doi:10.1007/s12613-019-1749-1.
17. Zheng D, Song W, Cao S, Li J, Sun L. Investigation on dynamical mechanics, energy dissipation, and microstructural characteristics of cemented tailings backfill under SHPB tests. Minerals. 2021;11(5):542. doi:10.3390/min11050542.
18. Han Z, Li D. Dynamic mechanical properties and wave propagation of composite rock-mortar specimens based on SHPB tests. Int J Min Sci Techno. 2022;32(4):793–806. doi:10.1016/j.ijmst.2022.05.008.
19. Xue G, Yilmaz E, Feng G, Cao S, Sun L. Reinforcement effect of polypropylene fiber on dynamic properties of cemented tailings backfill under SHPB impact loading. Constr Build Mater. 2021;279(1):122417. doi:10.1016/j.conbuildmat.2021.122417.
20. Selçuk L, Aşma D. Experimental investigation of the Rock-Concrete bi materials influence of inclined interface on strength and failure behavior. Int J Rock Mech Min Sci. 2019;123(7):104119. doi:10.1016/j.ijrmms.2019.104119.
21. Weilv W, Xu W, Jianpin Z. Effect of inclined interface angle on shear strength and deformation response of cemented paste backfill-rock under triaxial compression. Constr Build Mater. 2021;279(6):122478. doi:10.1016/j.conbuildmat.2021.122478.
22. Yu X, Song W, Tan Y, Kemeny J, Wang J. Energy dissipation and 3d fracturing of Backfill-encased-rock under triaxial compression. Constr Build Mater. 2022;341(1):127877. doi:10.1016/j.conbuildmat.2022.127877.
23. Yu X, Kemeny J, Tan Y, Song W, Huang K. Mechanical properties and fracturing of rock-backfill composite specimens under triaxial compression. Constr Build Mater. 2021;304(6):124577. doi:10.1016/j.conbuildmat.2021.124577.
24. Wang J, Fu J, Song W, Zhang Y. Mechanical properties, damage evolution, and constitutive model of rock-encased backfill under uniaxial compression. Constr Build Mater. 2021;285(68):122898. doi:10.1016/j.conbuildmat.2021.122898.
25. Si X, Gong F, Li X, Wang S, Luo S. Dynamic Mohr-Coulomb and Hoek-Brown strength criteria of sandstone at high strain rates. Int J Rock Mech Min Sci. 2019;115(4):48–59. doi:10.1016/j.ijrmms.2018.12.013.
26. Huang Z, Yilmaz E, Cao S. Analysis of strength and microstructural characteristics of mine backfills containing fly ash and desulfurized gypsum. Minerals. 2021;11(4):409. doi:10.3390/min11040409.
27. Zheng D, Song W, Cao S, Li J. Dynamical mechanical properties and microstructure characteristics of cemented tailings backfill considering coupled strain rates and confining pressures effects. Constr Build Mater. 2022;320(4):126321. doi:10.1016/j.conbuildmat.2022.126321.